

1 An unsteady pressure probe for the
2 measurement of flow unsteadiness in tidal
3 channels

4 Anna M Young *University of Bath*

5 Bath, United Kingdom

6 amy32@bath.ac.uk

7 Nicholas R Atkins *Whittle Laboratory*

8 *University of Cambridge*

9 Cambridge, United Kingdom

10 nra27@cam.ac.uk

11 Christopher J Clark *Whittle Laboratory*

12 *University of Cambridge*

13 Cambridge, United Kingdom

14 cjc95@cam.ac.uk

15 Gregory Germain *Ifremer*

16 Boulogne-sur-Mer, France

17 Gregory.Germain@ifremer.fr

18

Abstract

19

20

21

22

23

An unsteady five-hole probe has been developed for the measurement of turbulent flow in tidal channels. Such measurements are vital for accurate prediction of unsteady loads on tidal turbines. Existing field-based velocimeters are either unable to capture the required range of frequencies or are too expensive to profile the variation of turbulence across a typical tidal power site, and thus the available data is inadequate for turbine design.

24

25

26

27

This work adapts the traditional five-hole wind tunnel probe to achieve a low cost device with sufficient frequency range for tidal turbine applications. The main issue in the marine environment is that the ambient hydrostatic pressure is much higher than the dynamic pressure. This has been overcome by using novel calibration coefficients and differential transducers.

28

29

In flume tank tests against LDV measurements, the frequency response of the probe has been shown to be sufficient to capture all the frequencies necessary for tidal turbine design.

30

Index Terms

31

32

Velocity measurement, pressure, multi-hole probe, site assessment, tidal power, turbulence, unsteadiness

NOMENCLATURE

c	Wave propagation speed
f	Frequency
g	Acceleration due to gravity
K_{dyn}	Dynamic pressure calibration coefficient
K_{pitch}	Pitch calibration coefficient
K_{stag}	Total pressure calibration coefficient
K_{yaw}	Yaw calibration coefficient
LDV	Laser Doppler Velocimeter
p	Static pressure
p_0	Stagnation pressure
p_C	Centre-hole pressure
p_D	Bottom-hole pressure
p_L	Left-hole pressure
p_R	Right-hole pressure
p_U	Top-hole pressure
\bar{U}	Bulk flow speed
U_{probe}	Absolute velocity at probe
x	Streamwise co-ordinate
y	Transverse co-ordinate
z	Vertical co-ordinate
ϕ	Pitch angle
θ	Yaw angle

Acronyms

ADCP	Acoustic Doppler Current Profiler
ADV	Acoustic Doppler Velocimeter
CMRR	Common Mode Rejection Ratio

I. INTRODUCTION

34

35 Tidal turbines operate in a hostile environment - high turbulence levels, waves and large-
36 scale unsteadiness from geographical features combine to generate large fluctuating loads on the
37 turbine blades. Even small errors in unsteady load predictions at the design stage can lead to
38 large reductions in the fatigue life of components. To compound matters, flow conditions can
39 vary considerably even within one site. This means that tidal turbine designers need accurate
40 steady and unsteady flow data across all parts of every potential installation site.

41 The usual device for measuring tidal flows is the Acoustic Doppler Current Profiler (ADCP),
42 which is chosen for its ease of use - especially the fact that one device can scan across the full
43 depth of the channel while mounted on the seabed. However, it has been shown in previous
44 work by Guion and Young [1] that a standard ADCP cannot capture fluctuations smaller than
45 the radius of a typical turbine (10 m). By contrast, flow structures as small as half a blade chord
46 (0.5 m) are likely to cause unsteady loading issues. The unresolved lengthscales in ADCP data
47 could lead to an under prediction of the unsteady loading and therefore there is the potential for
48 unexpected mechanical failure.

49 Acoustic Doppler Velocimeters (ADV) could be used in place of ADCPs as they can capture
50 much smaller flow structures. However, they are less robust than ADCPs and take measurements
51 at a single location, meaning that multiple devices are required to give information about flow
52 variation with depth. Furthermore, both devices are too expensive to deploy at more than a few
53 locations across a site. There is, therefore, a need for a low cost, easily deployable device that
54 can capture unsteady velocity fluctuations with lengthscales of the order of half a blade chord.
55 Given the bulk convection speeds found in typical tidal channels, this translates to a minimum
56 frequency response of approximately 10 Hz.

57 The use of multi-hole pressure probes is commonplace in conventional turbomachinery re-
58 search. For applications where space constraints are not too onerous, fast-response versions have
59 been developed with the sensing components built into the probe head. Most recently, a fast-
60 response five-hole probe has been developed by Duquesne, Deschênes, Iliescu, and Ciocan [2],
61 and tested in small-scale, low hydrostatic head water pumps by Duquesne, Ciocan, Aeschlimann,
62 Bombenger, and Deschênes [3]. The major difference between their work and the application
63 discussed here is the background hydrostatic pressure, which is negligible in a small water pump,
64 but will be up to two orders of magnitude larger than the dynamic pressure in a typical tidal

65 channel. The hydrostatic pressure at depth in a tidal channel therefore dwarfs any changes in
66 pressure due to unsteady flow passing over the sensors.

67 Similarly, in a wind tunnel, the atmospheric pressure will be much larger than the dynamic
68 pressure, but this issue is overcome by using differential sensors with one side measuring a
69 reference such as the tunnel inlet pressure or the laboratory atmospheric pressure. The marine
70 environment, however, does not offer a convenient ‘reference’ pressure.

71 The prior art in the area of multi-hole pressure probes therefore suggests that the technology
72 could be transferred into the marine environment in order to provide unsteady flow measurements
73 if the high hydrostatic pressure can be accommodated without sacrificing accuracy. One solution
74 to the lack of reference pressure is to use differential measurements; this is the approach taken
75 in the work presented here.

76 This paper discusses the development of a marine five-hole probe. A prototype has been
77 manufactured and benchmarked against an LDV reference system in the flume tank at Ifremer,
78 Boulogne-sur-Mer, France. In the tests at Ifremer, the probe was shown to capture frequencies
79 up to 20 Hz accurately - more than sufficient for the calculation of unsteady loads on a tidal
80 turbine.

81 After an introduction to multi-hole probes (Section II), the key differences between tidal
82 channel flows and those encountered in wind tunnel testing will be discussed in Section III. The
83 novel calibrations required for taking measurements at depth will be derived in Section IV. After
84 this, key aspects of the probe design will be outlined in Section V, and the test setup will be
85 explained in Section VI. The calibration of the prototype probe will be described in Sections VII
86 and VIII. The steady flow accuracy and unsteady frequency response will then be discussed in
87 Sections IX and X, respectively, before improvements are discussed and conclusions drawn.

88 II. MULTI-HOLE PRESSURE PROBES

89 Multi-hole probes are commonly used in aerospace applications to make point measurements
90 of flow angles along with static and stagnation pressure. A section through a typical probe head
91 is shown schematically in Fig. 1. The centre, left and right holes are shown. On the left-hand
92 diagram, the probe is aligned with the flow; this means that the left and right holes will give
93 equal pressure readings, and the centre hole will register the stagnation pressure of the flow. If
94 the flow is at an angle to the probe, as shown on the right-hand diagram in Fig. 1, one of the

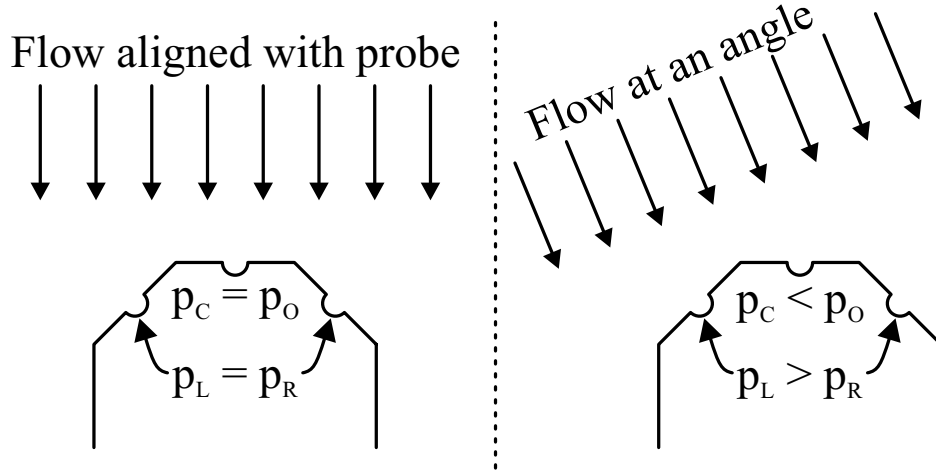


Fig. 1. Principles of operation of a five-hole probe.

95 side holes will read a higher pressure than the other, and the centre hole will no longer give the
 96 stagnation pressure.

97 By acquiring data with the probe at different yaw and pitch angles in a known, uniform flow,
 98 calibration maps can be generated, which give the relationship between flow direction and the
 99 relative hole pressures. The most commonly-used calibration coefficients, K , are:

$$100 \quad K_{\text{yaw}} = \frac{p_L - p_R}{p_C - \frac{1}{4}(p_L + p_R + p_U + p_D)} \quad (1)$$

$$101 \quad K_{\text{pitch}} = \frac{p_U - p_D}{p_C - \frac{1}{4}(p_L + p_R + p_U + p_D)} \quad (2)$$

$$102 \quad K_{\text{dyn}} = \frac{p_0 - p}{p_C - \frac{1}{4}(p_L + p_R + p_U + p_D)} \quad (3)$$

$$103 \quad K_{\text{stag}} = \frac{p_0 - p_C}{p_C - \frac{1}{4}(p_L + p_R + p_U + p_D)} \quad (4)$$

104 where p_L , p_R , p_U , p_D and p_C are the pressures recorded on the left, right, up, down and centre
 105 holes, respectively, p_0 is the flow stagnation pressure, and p is the flow static pressure.

106 The calibration maps derived from a known flow can be applied to data acquired in a wind
 107 tunnel test or in the aero-engine environment: the raw pressures from each hole are used to find
 108 K_{yaw} and K_{pitch} , and the calibration map is then inverted to find the yaw angle, θ , the pitch angle,
 109 ϕ , and therefore K_{dyn} and K_{stag} . Assuming incompressible flow, the velocity of the flow onto the
 110 probe is given by:

$$111 \quad U_{\text{probe}} = \sqrt{\frac{K_{\text{dyn}} \left(p_C - \frac{1}{4}(p_L + p_R + p_U + p_D) \right)}{\frac{1}{2}\rho}} \quad (5)$$

112 The streamwise, transverse and vertical velocity components are then found by converting from
 113 spherical polar to Cartesian co-ordinates:

$$114 \quad U_x = U_{\text{probe}} \cos \phi \cos \theta \quad (6)$$

$$115 \quad U_y = U_{\text{probe}} \cos \phi \sin \theta, \text{ and} \quad (7)$$

$$116 \quad U_z = U_{\text{probe}} \sin \phi \quad (8)$$

117 At high yaw/pitch angles (usually around 30° to 45°), the flow on one of the faces of the
 118 probe will separate; this causes a sharp drop in pressure on one face. The behaviour of the probe
 119 when the flow is separated can be highly dependent on Reynolds number, so researchers usually
 120 aim to use their probes only within the unseparated range, and it is preferable to ‘null’ the probe
 121 such that the side face pressures are equalised before measurements are taken, instead of relying
 122 on the accuracy of the extreme edges of the calibration map. This approach cannot, however, be
 123 taken in an unsteady flow environment, and so various adjustments to the calibration coefficients
 124 can be made to increase the accuracy of data at high angles [4].

125 III. SIZE AND SCALE CONSIDERATIONS

126 The typical ranges of conditions in tidal channels are compared with those encountered
 127 in aerospace applications in Table I (supersonic and hypersonic facilities are ignored in this
 128 analysis). It can be seen that the increase in density between air and seawater is offset by much
 129 lower flow speeds in the sea, such that the dynamic pressures expected in a tidal channel are
 130 comparable with the low speed end of typical wind tunnel test facilities. This, along with the
 131 blade Reynolds numbers being in the same range, suggests that similar measurement techniques
 132 will be appropriate for both flows. However, there are some major differences between the two
 133 applications: hydrostatic pressure, unsteady flow lengthscales and probe Reynolds number.

134 The main differences in measurement requirements between aero-engines and marine channels
 135 will now be discussed in turn.

136 A. Pressures

137 The hydrostatic pressure at 20 m depth (the hub height of a typical 1 MW turbine) will be
 138 almost 200 kPa, which is between 45 and 400 times larger than the dynamic head of the flow.

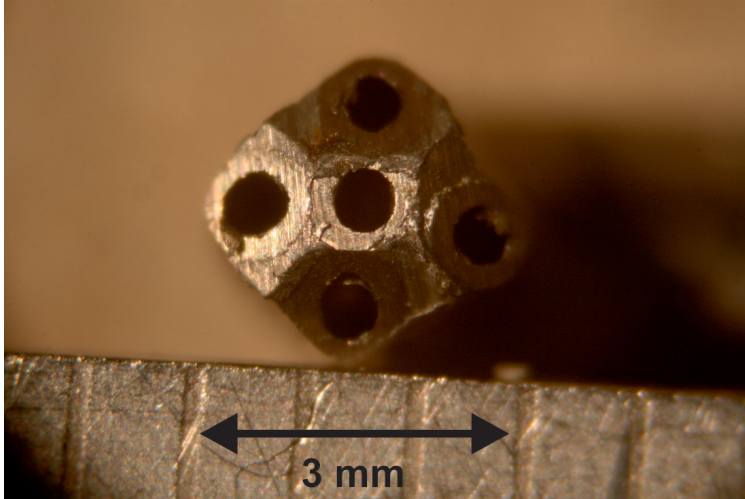


Fig. 2. Typical five-hole probe for wind tunnel applications (photo courtesy of James Taylor).

139 In order to measure the flow speed accurately, the dynamic pressure must therefore be isolated
140 from the hydrostatic pressure prior to measurement.

141 In wind tunnel testing, the atmospheric pressure is also far higher than the dynamic pressure,
142 and the issue of transducer sensitivity is solved by using differential sensors which are all
143 connected to the local atmospheric pressure (or the tunnel inlet static pressure). This straightfor-
144 ward technique allows sensors with a full-scale range similar to the dynamic head to be used,
145 as opposed to absolute transducers which would not be able to capture small changes in flow
146 speed.

147 Differential pressure transducers with full-scale range similar to the dynamic head are thus
148 essential in both wind tunnel and marine applications. There is, however, no convenient ‘refer-
149 ence’ pressure in the marine environment at depth and so the pressures on the probe faces must
150 be measured relative to one another. The exclusive use of differential transducers without an
151 independent reference pressure necessitates a novel set of calibration coefficients, which will be
152 discussed in detail in Section IV.

153 *B. Unsteady Flow Lengthscales and Frequencies*

154 In wind tunnel testing, researchers are usually interested in high-frequency, small-scale flow
155 features related to loss generation. In tidal turbine design, however, the major need is to capture
156 the unsteady flow structures in the channel. This means that the scales of interest are vastly
157 different in the two applications, as shown in Table I.

158 A tidal turbine designer needs information on unsteady flow structures down to scales equiv-
 159 alent to half the turbine chord in order to predict unsteady loading. This means that the flow
 160 features of interest range in size from 500 mm to 35 m. This makes it easier to manufacture a
 161 robust device and to mount the pressure transducers directly on the probe faces.

162 While miniature, high-frequency pressure transducers are generally manufactured to order in
 163 small batches, larger transducers with a lower frequency response are mass-produced for a wide
 164 range of applications. This therefore allows the use of lower cost components in the marine
 165 probe than in aerospace versions.

166 A further advantage of the large size of the probe is that geometric variation due to man-
 167 ufacturing tolerances will have a negligible impact on the calibration map. Work by Hall and
 168 Povey [5] has shown that, for a probe produced using additive manufacturing, the calibration
 169 map is unaffected by geometric defects due to tolerances as long as the probe diameter is above
 170 4 mm. This means that, for probes of the type discussed in this paper, individual devices would
 171 not have to be calibrated. Once a map of the type shown in Section VIII was produced for
 172 a given design, it would be universally applicable to all probes. This would drastically reduce
 173 costs, as performing a full yaw and pitch calibration for every device is a lengthy process¹.

174 *C. Probe Reynolds number*

175 The Reynolds number of the probe developed in this work (75 mm diameter) is compared
 176 with that of typical aerospace probes in Table I. It can be seen that there is an overlap in
 177 the range of Reynolds numbers experienced in the two applications. Work by Dudzinski and
 178 Krause [6] on fixed orientation probes, and their sensitivity to Reynolds number, showed that in
 179 some circumstances the probe must be calibrated at a series of different Reynolds numbers in
 180 order to obtain accurate data.

181 Building on this work, Dominy and Hodson [7] undertook a series of tests with different probes
 182 and at varying flow speeds. They found that the calibration map was approximately independent
 183 of Reynolds number when the probe Reynolds number was above 15×10^3 , which is 5 times less
 184 than the Reynolds number of the prototype probe discussed here. Their work therefore means
 185 that the prototype probe developed here is expected to give readings that are independent of
 186 Reynolds number. This will be examined in Section VI.

¹The electronic components will still need calibration, as outlined in Section VII, but this is a far quicker, cheaper process than the yaw and pitch calibration

TABLE I
COMPARISON OF FLOW PROPERTIES FOR TIDAL AND WIND TUNNEL APPLICATIONS.

Quantity	Tidal	Wind tunnel
Working fluid		
Density (kg/m ³)	997	1.225
Kinematic viscosity (m ² /s)	1.0×10 ⁻⁶	1.6×10 ⁻⁵
Flow speed (m/s)	1 – 3	30 – 300+
Reynolds numbers		
Typical blade chord (m)	1	0.05
Typical blade Reynolds number	1 – 3×10 ⁶	0.1 – 1×10 ⁶
Typical probe diameter (mm)	75	1 – 10
Typical probe Reynolds number	75 – 230×10 ³	2 – 100×10 ³
Pressures		
Depth (m)	10 – 80	n/a
Hydrostatic pressure (gauge, kPa)	99 – 790	n/a
Dynamic pressure ($p_0 - p$, kPa)	0.49 – 4.5	0.55 – 55
Lengthscales		
Flow lengthscales of interest	0.5 – 35 m	1 – 50 mm
Max. frequency of interest (Hz)	10	50000+
Kolmogorov microscale (μm)	50 – 100	1 – 8

IV. NEW CALIBRATION COEFFICIENTS

187

188

189 In order to overcome the twin issues of high ambient hydrostatic pressure and a lack of a
190 local reference pressure, differential transducers must be used between the probe faces. This, in
191 turn, requires a novel set of calibration coefficients. Each transducer measures the difference in
192 pressure between the centre hole and one of the four side holes. Using these novel coefficients,
193 the yaw and pitch angles can be calculated as with a conventional probe, and the dynamic
194 pressure can be found. It can be seen that the conventional yaw coefficient:

$$195 \quad K_{\text{yaw}} = \frac{p_L - p_R}{p_C - \frac{1}{4}(p_L + p_R + p_U + p_D)} \quad (9)$$

196 can be obtained using differential signals via the following mathematically equivalent expression:

$$197 \quad K_{\text{yaw}} = \frac{(p_C - p_R) - (p_C - p_L)}{\frac{1}{4}[(p_C - p_L) + (p_C - p_R) + (p_C - p_U) + (p_C - p_D)]} \quad (10)$$

198 Similar expressions for the pitch coefficient, K_{pitch} , and the dynamic coefficient, K_{dyn} , can also
 199 be found:

$$200 \quad K_{\text{pitch}} = \frac{(p_C - p_D) - (p_C - p_U)}{\frac{1}{4}[(p_C - p_L) + (p_C - p_R) + (p_C - p_U) + (p_C - p_D)]} \quad (11)$$

$$201 \quad K_{\text{dyn}} = \frac{p_0 - p}{\frac{1}{4}[(p_C - p_L) + (p_C - p_R) + (p_C - p_U) + (p_C - p_D)]} \quad (12)$$

202 As shown in Section II, the calibration map can be inverted to find the pitch and yaw angles
 203 and then the flow speed can be derived from the dynamic coefficient and Bernoulli's equation (as
 204 the flow is incompressible). The total pressure coefficient, however, cannot be derived from the
 205 differential measurements available. This means that the absolute static and stagnation pressures
 206 cannot be found (unless an additional, absolute transducer is fitted). This is not of concern in
 207 the current work, as the quantities of interest are flow speed and direction, for which the yaw,
 208 pitch and dynamic coefficients are sufficient.

209 V. PROOF OF CONCEPT PROTOTYPE

210 The prototype probe is shown schematically in Fig. 3(a). The probe diameter is 75 mm and
 211 the distance from the front of the probe to the right-angle in the stem is approximately three
 212 diameters. The prototype was built using low-cost commodity components and rapid-prototyped
 213 parts.

214 Unlike a wind tunnel probe, the marine device has to survive in a corrosive fluid (sea water)
 215 at high pressure. The probe in Fig. 3 was made from four parts which were 3D printed using a
 216 polymer with similar properties to ABS or polypropylene (depending on the life-span required,
 217 production models could be machined from marine-grade stainless steel).

218 It can also be seen from Fig. 3(a) that the prototype has a conventional five-hole probe head,
 219 with two design features suggested by Dominy and Hodson [7]. Firstly, the faces are at 45° to
 220 one another and have sharp edges. This design gives superior performance to a cone-type probe
 221 at high yaw and pitch angles. Secondly, the holes are perpendicular to, and at the centre of, each
 222 face - moving the holes back from the front edge reduces the effect of Reynolds number on the
 223 probe calibration map. Ainsworth, Allen and Batt [8] found that the optimal hole position is not
 224 necessarily at the centre of the face. However, the holes are central on the prototype for ease of
 225 construction.

226 An internal section view of the probe is given in Fig. 3(b). It can be seen that the device
 227 has on-board amplification and that there is sufficient space within the body for on-board data

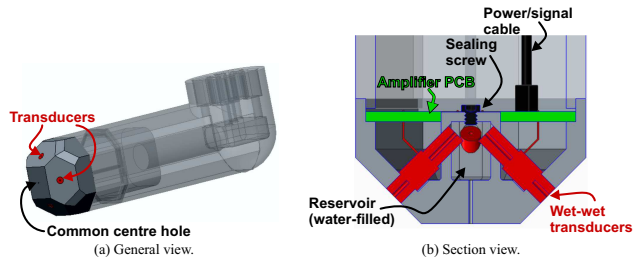


Fig. 3. Drawing of probe head design and transducer location.

228 acquisition and a battery, as is common in marine measurement devices. For the purpose of this
 229 test, however, a standard laboratory grade data acquisition system was used, mounted immediately
 230 above the water surface, connected to the probe by 3 m cables and controlled by a desktop PC.
 231 The electronic components are protected from exposure to water, with the exception of the
 232 transducers, which are wet-wet and are exposed to water on both sides of their diaphragms.

233 The pressure sensors (shown in red) are low-cost commercial-off-the-shelf wet-wet differential
 234 transducers with a full scale range of 7 kPa (to the authors' knowledge, this was lowest range
 235 wet-wet transducer available with sufficiently small dimensions). Although 7 kPa is appropriate
 236 for a typical tidal channel flow, the flume tests were run at 0.8 m/s, which is at the low end of
 237 expected field conditions. As a result, the peak dynamic head in the flume is only about 0.5 kPa.
 238 In addition, the transducers have a full scale output of 16.7 mV, which is relatively low. In order to
 239 generate usable data from such small signals, a low noise, high CMRR instrumentation amplifier
 240 (shown in green) was fitted within the probe head. The amplifier had a differential gain of 200,
 241 and a line driver was incorporated into a custom PCB which was fitted immediately behind the
 242 transducers.

243 The transducers are mounted directly in the holes on the faces, with the minimum possible tube
 244 length between the probe face and the sensing diaphragm. The four rear ports of the transducers
 245 are immersed in a reservoir which is connected to the centre hole of the probe. This means that
 246 each transducer will measure the difference between the centre hole and one of the side holes,
 247 thus eliminating the hydrostatic pressure as described in Section IV.

248 Not shown in Fig. 3 are the reference thermocouples, which are used to provide temperature
 249 compensation for the pressure transducers, and a copper heat sink which ensures constant
 250 temperature across the probe head even if there is a temperature gradient in the flow.

251 As water is considered incompressible, the reservoir should have a negligible effect on the

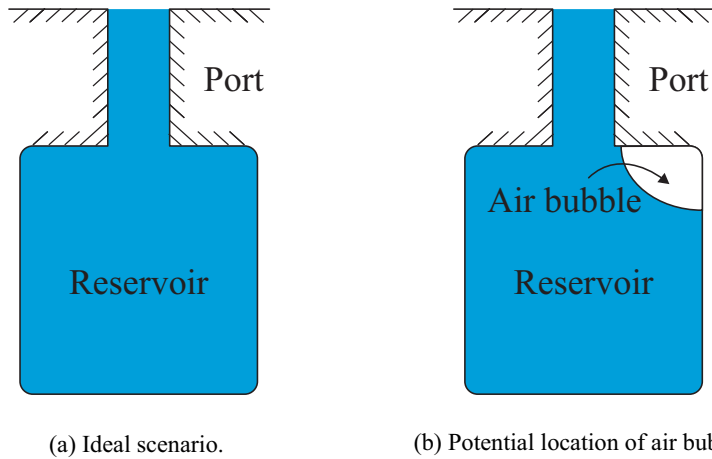


Fig. 4. Pressure port and reservoir as a Helmholtz resonator with and without air bubble.

252 frequency response over the range of frequencies and pressures considered here. However, the
 253 presence of an air bubble anywhere between the probe faces and the transducer diaphragms
 254 is likely to introduce a resonant response. In order to prevent this, the centre hole was sealed
 255 temporarily, and the probe orientated with the centre hole facing downwards. Whilst in this
 256 configuration, the reservoir and the transducer ports were filled with water using a syringe. This
 257 process was repeated over a period of several hours to allow air bubbles to rise to the surface.

258 Once the reservoir was full and free of air bubbles, the sealing screw was inserted and the
 259 centre hole was re-opened at the same time to prevent overpressure. The front ports of the
 260 transducers were also filled with water in a similar manner. Care was taken to keep the reservoir
 261 and ports full during transit and installation.

262 The impact of an air bubble in the reservoir on the frequency response can be estimated by
 263 considering the pressure ports and reservoir as Helmholtz resonators. The corresponding resonant
 264 frequencies are given in Table II. It can be seen that, for the ideal case, where the reservoir and
 265 the port are both completely filled with water, the Helmholtz resonance frequency is 20 kHz,
 266 which is 3 orders of magnitude higher than the frequencies of interest. Introducing even a small
 267 air bubble, however, reduces the resonant frequency considerably. The worst-case scenario is
 268 when the port is completely water-filled, but the reservoir is completely air-filled. This gives a
 269 resonant frequency of 16 Hz. From the information in Table II, it can be seen that the resonant
 270 frequency will be higher than 50 Hz as long as the reservoir is at least 90% filled with water.
 271 This is achievable with the method described above.

TABLE II
HELMHOLTZ RESONANCE FREQUENCIES FOR PORTS AND RESERVOIR WITH DIFFERENT LEVELS OF WATER.

Percentage of reservoir filled with water	Percentage of port filled with water	Helmholtz frequency (Hz to 2 s.f.)
100	100	20000
0	0	470
0	100	16
50	100	23
70	100	30
80	100	36
90	100	51
95	100	73
98	100	110

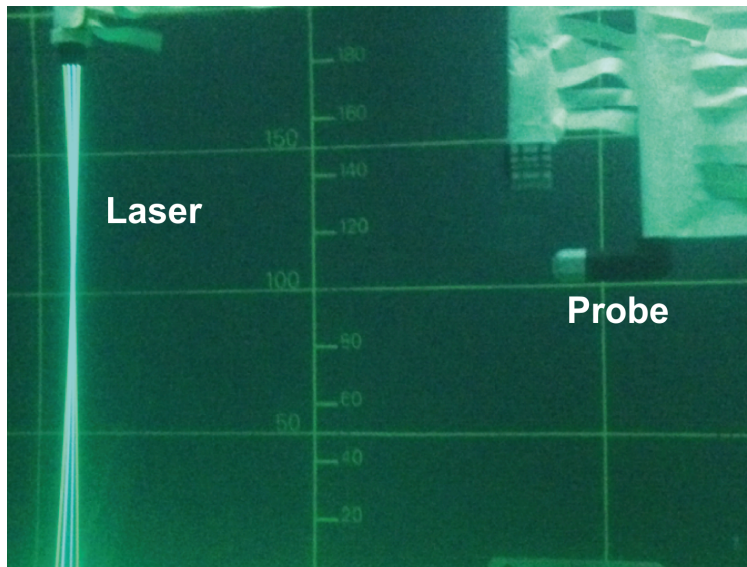


Fig. 5. Test setup in flume tank at Ifremer with LDV upstream of prototype probe.

VI. TEST SETUP

272

273 The probe was tested in the flume tank at Ifremer, Boulogne-sur-Mer, France. The flume
 274 has a working section which is 2 m deep by 4 m wide and a background turbulence level
 275 of approximately 5%. The tank is equipped with wave maker paddles for combined wave and
 276 current testing. The maximum nominal flow speed is 1.6 m/s with clean flow and 0.8 m/s with
 277 waves.

278 Measurements from the reference LDV system (see below) showed that the mean speed was
279 controlled to within $\pm 1\%$ of the nominal flow speed without waves. It is known that the flow is
280 slightly faster at mid depth when waves are being generated (see [9]), and this can be seen in
281 Fig. 11, where the nominal flow speed is 0.8 m/s but the probes are both measuring an average
282 flow speed of 0.9 m/s. For further details of the test facility and the uniformity of the flow in
283 the test section with and without waves, see [9] and [10].

284 A photo of the test setup is shown in Fig. 5. The probe was fitted centrally at mid-depth in
285 the flume and tested in flow speeds of 0.4 to 1.6 m/s in clean flow, and at 0.8 m/s with 0.5 Hz
286 surface waves (100 mm wave height).

287 *A. Probe Setup*

288 The probe-holder was designed such that the probe head could be yawed from -45° to $+45^\circ$,
289 but mounting constraints meant that the pitch angle could only be adjusted to three levels (0, 6.3°
290 and 12.2°). This allowed a full yaw calibration to be undertaken and a limited pitch calibration.
291 A probe of this size is expected to be symmetrical, as manufacturing errors will be negligible,
292 and so the only asymmetry is expected to be in the pitch direction. This asymmetry will be
293 due to the effect of the probe stem (which may divert the flow and thus induce a slight pitch
294 angle onto the probe), and due to the difference in hydrostatic pressure between the top and
295 bottom holes (which is approximately 500 Pa for the probe tested here). This asymmetry will
296 be discussed in Section VIII.

297 In order to compare the calibration with the expected behaviour of the probe, the data will be
298 compared with two models. First, results will be used from a RANS simulation of the probe head
299 (i.e. without the stem) at pitch and yaw angles from -20° to $+20^\circ$. Second, the inviscid model
300 of Zilliac [11] will be plotted, using the streamline projection method of Chondrokostas [12].

301 The unsteady data shown in this paper is from 240-second long samples; this corresponds to
302 approximately 20 tank through-flow times. The sample rate for the probe was set to 10 kHz in
303 order ensure that the data was over-sampled and to allow for filtering at a later point.

304 *B. Flow Reference Measurements*

305

306 In all tests, a Laser Doppler Velocimeter (LDV) was set up 2.5 m upstream of the probe and
307 data acquisition was undertaken simultaneously so as to provide reference measurements. The

LDV system could only record the axial and transverse velocity components, while the five-hole probe recorded all three velocity components (axial, transverse and vertical). In a separate test, the LDV was repositioned and the vertical component of the flow was measured with waves.

The LDV system available at Ifremer is 2 dimensional, i.e. composed of 4 laser beams with 2 different wave lengths: 514 nm and 488 nm. The measurement volume is 2.51 mm long and the laser beam thickness is 0.12 mm (giving a volume of 0.01 mm³). This is a smaller sampling volume than that of the probe, where it is assumed that the flow is uniform over the probe head (75 mm in each direction). This difference in sampling volume should not be an issue for the work presented here because the fluctuations in the flow are negligible over lengthscales of the size of the probe head.

The water in the tank is seeded with particles of silver-coated glass with a typical diameter of 10 μm ; this should be small enough to follow the flow, yet large enough to scatter sufficient light to obtain a good signal-to-noise ratio.

The mean sample rate of the LDV was 540 Hz in the axial direction and 240 Hz in the transverse direction, but this rate varied in both directions due to the random rate at which particles crossed the sample volume.

In order to compute the power spectral density and autocorrelation of the LDV data, it is usually necessary to re-sample at a constant sample rate. The LDV spectra shown here have been computed by using a zeroth-order sample and hold technique, as advocated by Tropea and Yarin [13], with the re-sampling rate set to the minimum LDV sample rate (approximately 50 Hz in the streamwise direction and 20 Hz in the transverse direction), in order to avoid artificial alterations to the spectra obtained.

VII. TRANSDUCER CALIBRATION AND DRIFT

The pressure transducers mounted in the probe head give an analogue signal in Volts. This signal is recorded via an Analogue-to-Digital converter and must then be converted into pressure in Pascals before the calibration coefficients described in Section VIII are used to find the flow speed and direction. For the transducers used in this study (Omega PX26 wet-wet differential sensors), pressure and voltage should be related linearly:

$$P = A(V - V_0) \quad (13)$$

where P is the pressure on the probe face, V is the voltage given by the transducer, A is the calibration gradient (given in Pascals per Volt) and V_0 is the voltage recorded when there is no

339 pressure difference across the transducer. The zero-pressure voltage is determined by the error
340 in resistance of the resistors making up the Wheatstone bridge circuit inside the transducer, and
341 will change with temperature. The effect of temperature on V_0 and the calibration gradient, A ,
342 will now be shown.

343 The effect of temperature on the zero-pressure voltage, V_0 , is shown in Fig. 6(a). Results
344 for two transducers are shown, to illustrate the variability between sensors. It can be seen that
345 the zero offset varies from one transducer to the next, and that changing the temperature of the
346 transducer creates an approximately linear change in the zero-pressure voltage. In an environment
347 where temperature changes were expected, the thermocouples in the probe head could be used
348 to correct the readings. In all the results shown in this paper, the zero level was measured at the
349 start and end of each experiment and the temperature changes were negligible during any given
350 experiment ($< 0.2^\circ\text{C}$). The flow speed was found to have no effect on the temperature measured
351 inside the probe head.

352 Figure 6(b) shows the response of the same two sensors to changes in pressure (both positive
353 and negative) at two temperatures. The maximum pressure used (450 Pa) is the dynamic head
354 of water flowing at 1.0 m/s (i.e. far smaller than the range of the sensors, which is 6700 Pa).
355 Considering first the calibrations at 16°C (black and red lines), it can be seen that the calibration
356 gradients are slightly different between the two sensors, and that sensor 1 has a more linear
357 response than sensor 2 (the black squares lie closer to the linear fit line than the red squares).
358 When the calibration was repeated at 30°C (green and blue lines), more points were recorded
359 in the range near zero pressure. Two things can be observed: first, there is little or no change in
360 the calibration gradient with temperature. Second, sensor 2 shows significant non-linearity over
361 the range 0-200 Pa. This is a departure from the ideal behaviour but is within the manufacturer's
362 specification and highlights the issues arising when sensors are used over only 10% of their
363 specified range. The calibration applied to the data to convert from voltage to pressure can be
364 adapted to account for this non-linearity, or higher accuracy transducers can be used.

365 Not considered here are any effects on the calibration of a common-mode offset caused by
366 the transducer being at depth. This may change both the zero offset and the calibration gradient
367 of the transducers. In the tests shown below, the zero levels of the transducers were measured
368 with the probe installed in the flume tank, to minimise any common-mode errors.

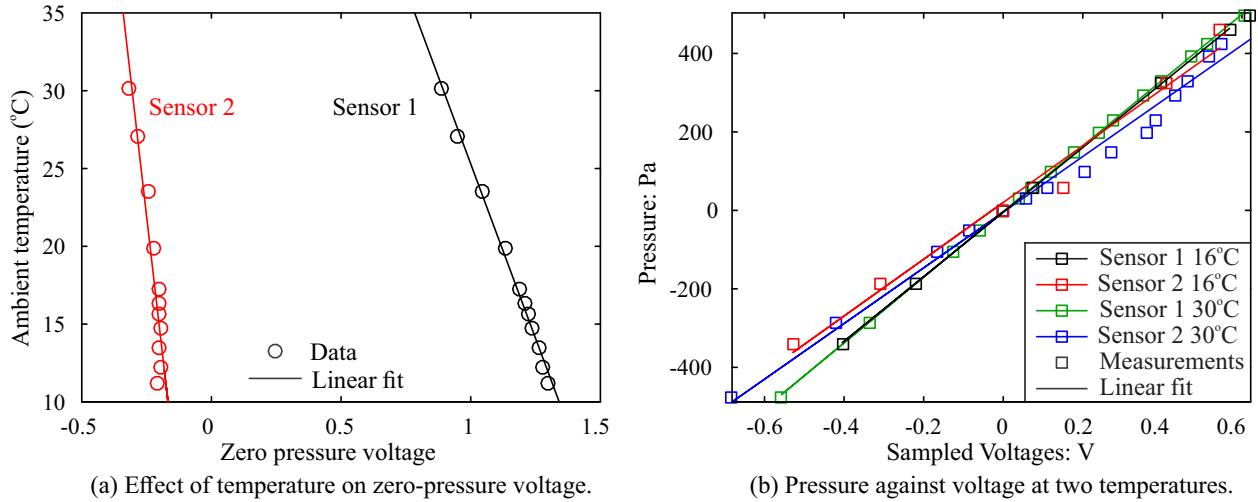


Fig. 6. Pressure transducer calibration (two sensors shown).

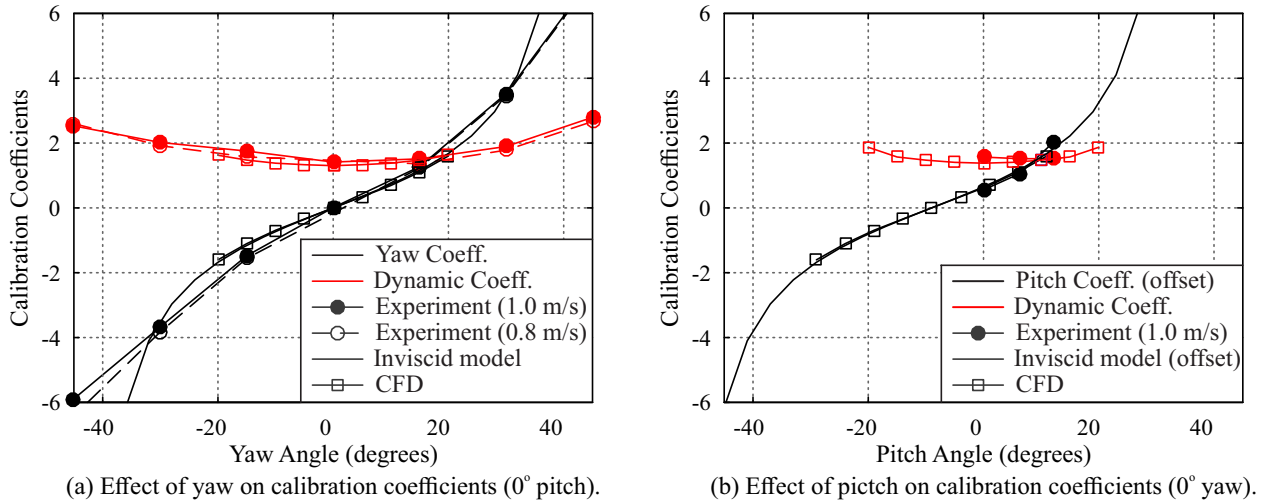


Fig. 7. Calibration coefficients against yaw and pitch angle.

VIII. STEADY FLOW YAW AND PITCH CALIBRATION

369

370 The second stage in the calibration process is to convert the four differential pressure mea-
 371 surements ($p_C - p_L$, $p_C - p_R$, $p_C - p_U$ and $p_C - p_D$) into flow speed and direction using the calibration
 372 procedure described in Section IV. In order to do this, the calibration coefficients must be recorded
 373 at different yaw and pitch angles to produce a calibration map. The map will be discussed in
 374 this section.

375 The calibration coefficients are shown in Fig. 7(a) as a function of yaw angle for tests with
 376 flow speeds of 0.8 m/s and 1 m/s, and as a function of pitch angle in Fig 7(b). The calibration

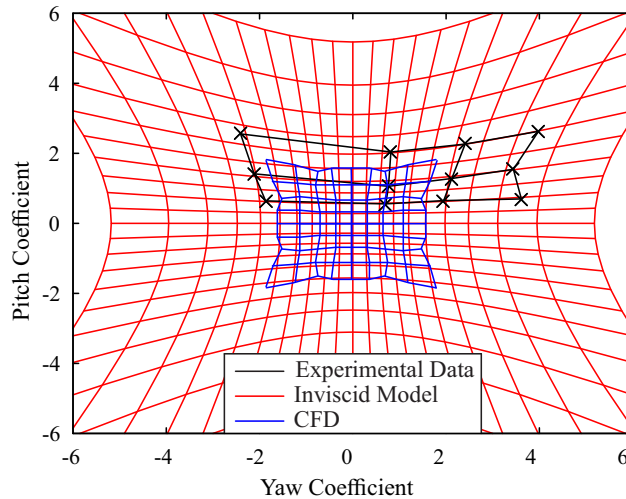


Fig. 8. Pitch coefficient against yaw coefficient (1.0 m/s flow speed).

377 data (large circles) is compared with a set of RANS CFD solutions for the probe (squares) and
 378 against the inviscid, analytical solution of Zilliac [11] (using the streamline projection method
 379 of Chondrokostas [12]) for yaw and pitch coefficient (solid lines).

380 It can be seen that the probe behaves as expected: the dynamic pressure coefficient is approx-
 381 imately constant for angles less than $\pm 20^\circ$, while the yaw coefficient is linear over the same
 382 range. There is good agreement between the experimental data, the CFD and the analytical
 383 solution over smaller angles. At larger yaw angles, separation on whichever face is at the most
 384 extreme angle to the flow causes the coefficients to deviate. This causes disagreement between
 385 the inviscid model and the probe data at yaw angles of $\pm 45^\circ$.

386 Constraints in the experimental setup meant that it was only possible to test the probe at
 387 three different pitch angles: 0° , 6.3° and 12.2° . The pitch coefficient is not zero at zero pitch.
 388 This is due to the effect of the probe stem meaning that the probe records a pitch coefficient
 389 equivalent to 9° of pitch at zero degrees. In Fig. 7(b), the CFD and analytical solutions for
 390 pitch coefficient have been shifted by 9° to account for these effects. As with the yaw angle
 391 behaviour, the agreement between the experiment and the models is good and the pitch and
 392 dynamic coefficients follow the expected trends.

393 The hydrostatic pressure gradient in water ($\frac{\partial P}{\partial z} = \rho g$) is approximately 9800 Pa/m, giving a
 394 difference in pressure between the top and bottom holes of approximately 500 Pa (and this head
 395 difference will be identical inside the probe assuming a water-filled reservoir). In the results

396 shown here, this has been accounted for in the zero-flow voltage measurements taken at the start
 397 of each experiment. In a tidal channel, where the hydrostatic pressure gradient will vary with
 398 temperature, depth and salinity, an additional differential measurement could be used to find the
 399 local gradient.

400 Another way to visualise the calibration coefficients is to plot the pitch coefficient against
 401 yaw coefficient so that the combined effect of yaw and pitch can be seen. This has been done
 402 in Fig. 8. The red grid shows the results from the inviscid model, while the CFD calculations
 403 are shown in blue and the black crosses show the experimental data. It can be seen that the
 404 agreement between the two models and the experiments is good.

405 Returning to Fig. 7(a), there is very little variation between the yaw and dynamic coefficient
 406 curves for the two flow speeds. This suggests that Reynolds number effects are minimal (at least
 407 over the speed range tested here). This is in line with the findings of Dominy and Hodson [7],
 408 who showed that Reynolds number effects are only important for probe Reynolds numbers below
 409 15×10^3 , far lower than the Reynolds numbers in typical tidal channels (see Table I).

410 The best way to minimise errors due to Reynolds number sensitivity and data uncertainty is
 411 to avoid using the probe at high angles of attack where one face is separated. This is usually
 412 achieved by ‘nulling’ the probe such that it faces the bulk flow direction.

413 In situations where this is not possible - due to high levels of unsteadiness, or the probe
 414 being fixed (both of which will be true in a tidal channel) - the angle range of the probe can
 415 be improved by changing the denominator of the calibration coefficients. There are numerous
 416 permutations in the literature, including those of Dunkley [4], who used a weighting factor to
 417 bias the denominator towards the holes which were closest to the local stagnation pressure.

418 IX. ACCURACY OF STEADY VELOCITY MEASUREMENTS

419 The calibration from above can now be applied to measured data to assess the accuracy of the
 420 probe. The test data used for this purpose is from a series of tests at seven different flow speeds
 421 from 0.4 m/s to 1.6 m/s and from six independent tests at 0.9 m/s. Measurements were averaged
 422 over tens of thousands of samples so that the precision error is negligible, and the errors found
 423 will be the cumulative bias error from the transducer measurement and the calibration map.

424 The main error is expected to be from the transducer bias error, which is quoted by the
 425 manufacturer as 1% of full scale (i.e. 69 Pa or 15% of the dynamic head in water at 1.0 m/s).
 426 This bias error can be reduced by calibrating each transducer as described in Section VII. This

427 process will eliminate errors due to variations in sensitivity or linearity, and will account for
428 the dependence of zero pressure voltage on temperature. Any drift in the zero level during tests
429 will, however, introduce significant errors and it will be shown that this drift dominates the total
430 error.

431 Prior to the accuracy tests discussed here, it was found that there was an offset between the
432 measured probe velocity and the true flow speed. This was corrected by applying a voltage offset
433 of 25 mV to the zero level of each transducer, both for the calibration described above and for
434 the data shown in Figs. 9 and 10 (i.e. $P = A(V - V_0 + 0.025)$). The reasons for this offset are
435 unclear, but it appears that the zero pressure voltage changes when the flume tank is switched
436 on (there is no change in temperature, so it is not due to a lack of temperature compensation).

437 Figure 9 shows measured velocity against true flow velocity from tests at seven different flow
438 speeds. The red line represents zero error, while the blue dashed lines show error bands of $\pm 5\%$.
439 The red dots are the data, to which a zero level offset of 25 mV has been applied as described
440 above. It can be seen that all the red dots lie within the 5% error band, with the exception of
441 the 0.4 m/s case. This gives a lower bound on the flow speeds that can be measured with the
442 probe, as the dynamic head becomes too small to record accurately ($P_0 - P$ is approximately
443 450 Pa at 1 m/s and only 72 Pa at 0.4 m/s).

444 The errors in measured flow speed for six independent tests at 0.9 m/s are shown in Fig. 10.
445 Tests 1-4 were undertaken with waves present at 0.5 Hz, while tests 5-6 were undertaken in
446 clean flow. Again, an offset of 25 mV has been applied to the measured zero pressure voltage. It
447 can be seen that the scatter in the data is small (less than 2% of the mean flow speed), but that
448 there is an offset of 5-10% in the flow speed. Applying a further offset of 12 mV to the data
449 gives the red dots - all within $\pm 1\%$ of the real flow speed ((i.e. $P = A(V - V_0 + 0.037)$). Once
450 again, transducer drift is the main source of the error in the steady flow velocity measurements.

451 From this data, it can be concluded that the errors in mean flow speed are due to drift in the
452 zero-pressure voltages given by the transducers. The offset in the zero level is not understood,
453 as zero levels were recorded immediately prior to running the experiments and there was no
454 appreciable temperature change. The data also shows that the lower bound of speeds which can
455 be measured to $\pm 5\%$ is 0.6 m/s. Using higher specification transducers would improve the steady
456 flow accuracy of the probe; the problem shown here is not inherent to the probe design.

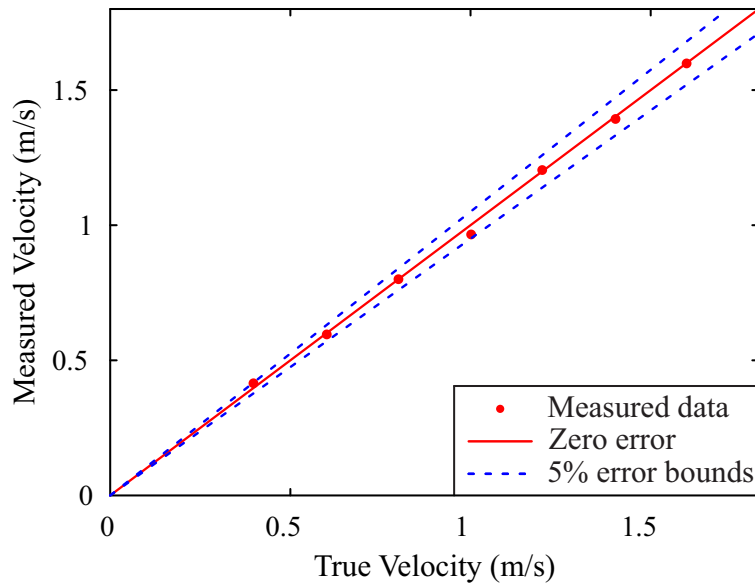


Fig. 9. Measured flow speed against actual flow speed (with corrected zero levels).

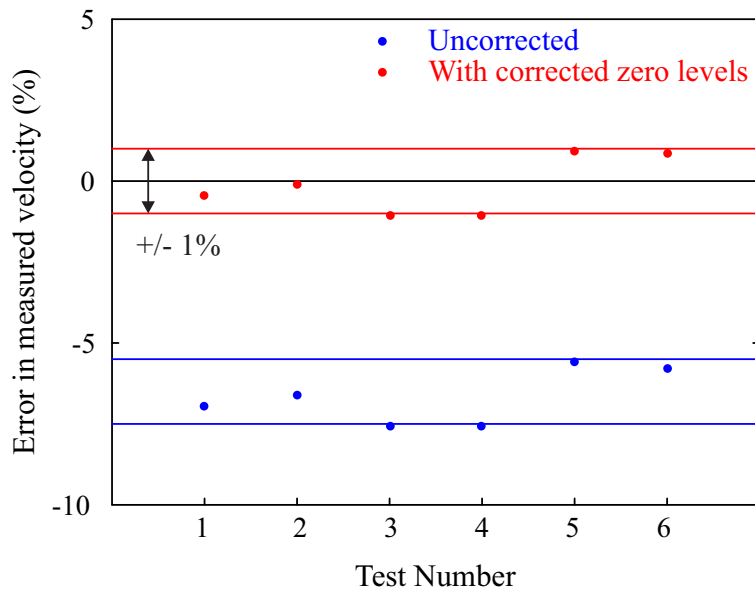


Fig. 10. Error in measured flow speed from six tests at 1.0 m/s with and without zero level correction.

457

X. UNSTEADY FLOW MEASUREMENT COMPARISON

458

459

460

The main aim of this work is to show that the probe can resolve unsteady flow features of the scales relevant to tidal turbine designers (0.5 to 35 m, or frequencies up to 10 Hz). This will be shown now with data taken from the probe and the reference LDV described in Section VI-B

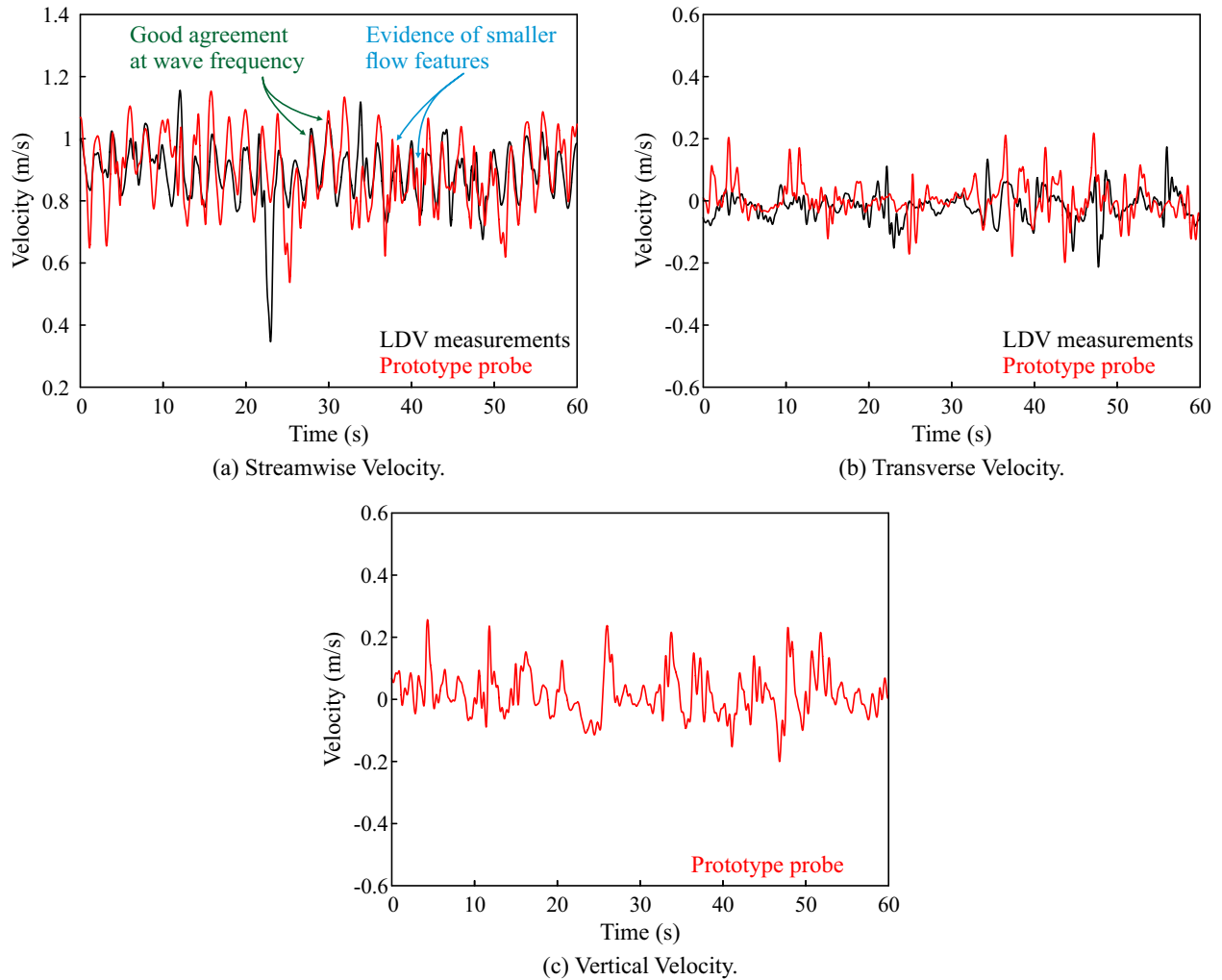


Fig. 11. Comparison of raw signals from LDV and prototype probe (0.8 m/s average flow speed, with waves at 0.5 Hz).

461 both with and without waves.

462 Constraints in the flume tank mounting arrangement mean that there was a spatial offset (2.5 m)
 463 between the LDV and the probe. This offset means that it is necessary to shift the signals in
 464 time in order to compare unsteady velocity measurements. However, different flow structures
 465 will convect at different speeds and so it is not possible to compare all flow structures directly
 466 between the two measurements. The two primary speeds at which structures may convect are
 467 the bulk flow speed, \bar{U} , and the speed of the surface waves, which is given by:

$$468 \quad c = \bar{U} \pm \frac{g}{2\pi f} \quad (14)$$

469 where f is the frequency of the waves. The propagation speeds of other structures are unknown,
 470 and new small structures are likely to evolve between the two measuring locations.

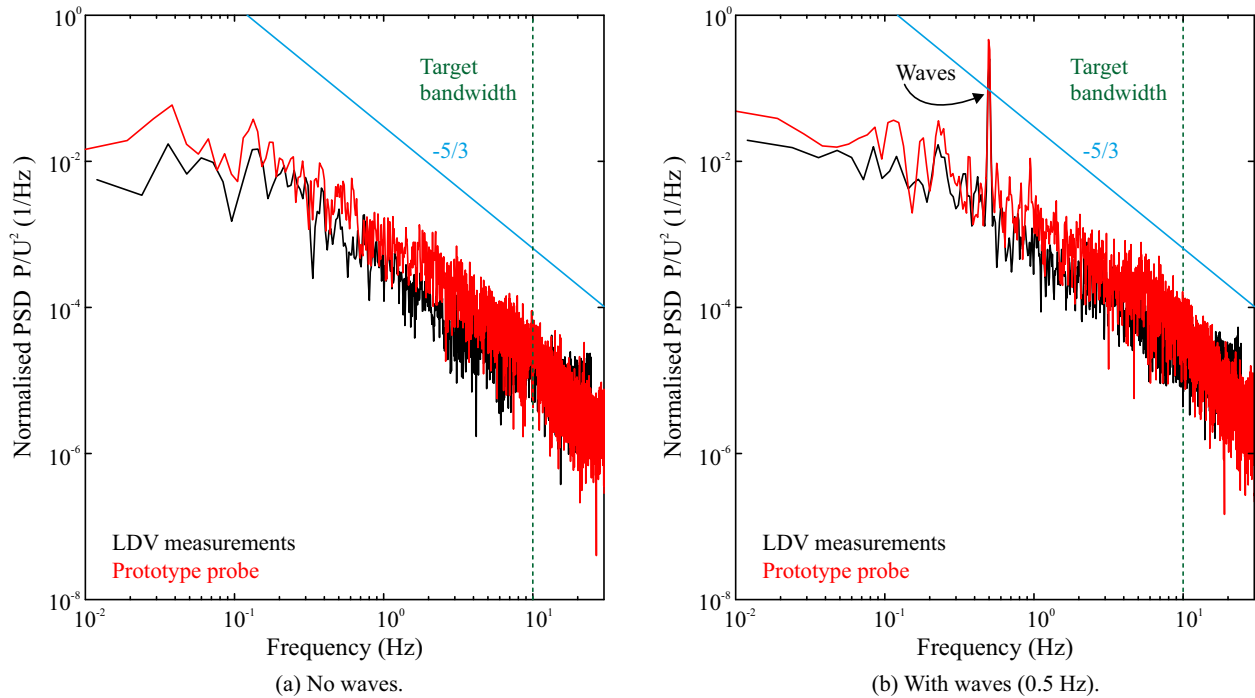
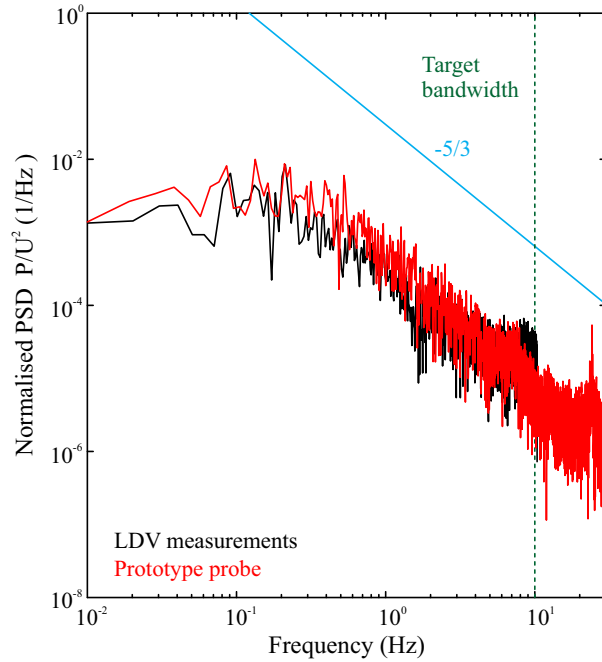


Fig. 12. Comparison of power spectral density of streamwise velocity from five-hole probe with LDV measurements with and without waves (0.8 m/s).

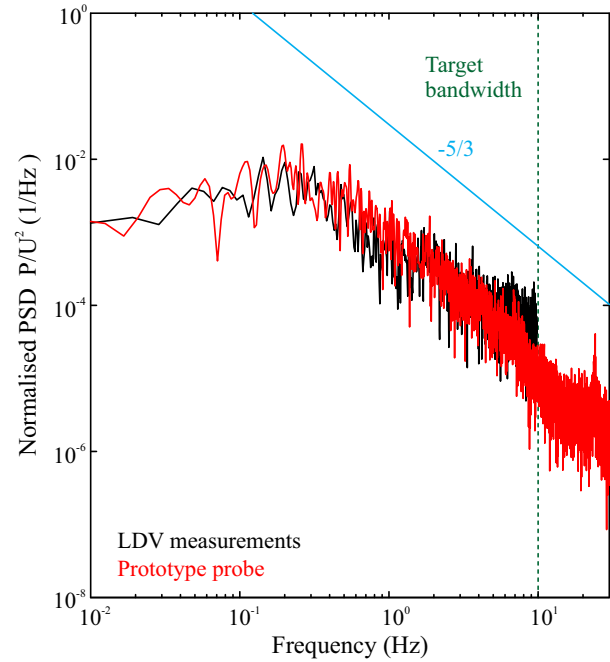
471 A comparison of the streamwise flow velocity from the two devices is given in Fig. 11 (a),
 472 with a temporal shift (based on the wave propagation speed) applied to account for the spatial
 473 offset between probes. The data shown is from a test at 0.8 m/s with waves at 0.5 Hz. In
 474 order to enable comparison of the unsteadiness captured at and around the wave frequency, both
 475 measurements have been filtered to remove all content above 2 Hz. It can be seen that both the
 476 LDV (black line) and the probe (red line) capture the waves, and that they agree on the longer
 477 time-scales of unsteadiness in the tank. The higher frequencies indicate the presence of smaller
 478 turbulent flow structures, which will not be constant between the two locations. However, in
 479 periods when higher frequencies are absent, the agreement is good.

480 Figures 11(b) and (c) show the transverse and vertical velocities respectively. It can be seen
 481 that the magnitude of the fluctuations in transverse velocities agrees well between the LDV and
 482 probe measurements. The LDV system was not set up to record the vertical velocity, but the
 483 vertical velocity recorded by the probe is shown in Fig. 11(c) for completeness.

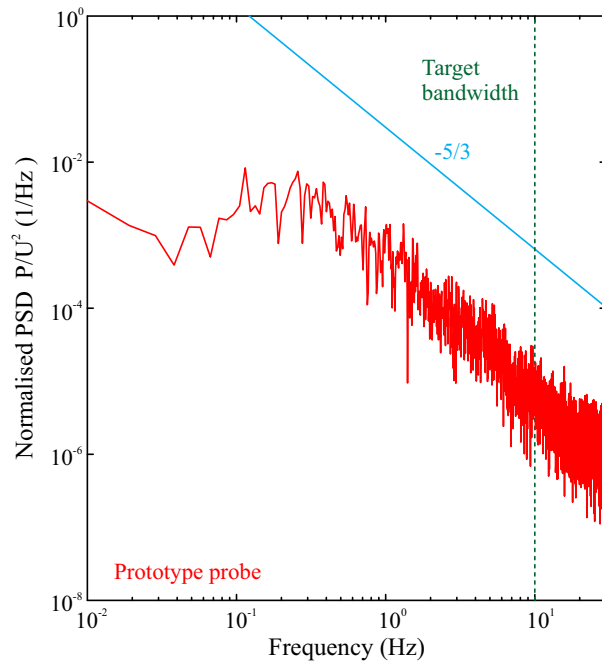
484 Although it is not reasonable to expect that individual gusts are frozen as they convect from
 485 the LDV measurement location to the probe, the flow is likely to be statistically similar, if not



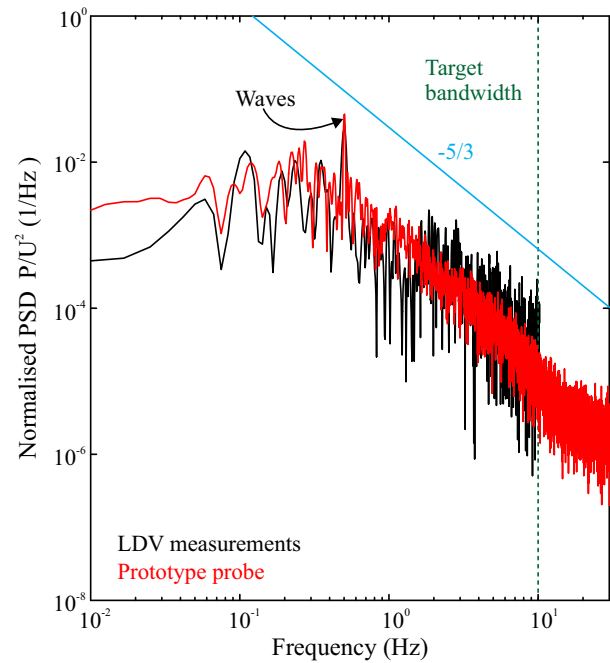
(a) Transverse direction, no waves.



(b) Transverse direction, with waves (0.5 Hz).



(a) Vertical direction, no waves.



(b) Vertical direction, with waves (0.5 Hz).

Fig. 13. Comparison of transverse and vertical power spectral density from five-hole probe with LDV measurements with and without waves (0.8 m/s).

486 homogeneous, between the two points. Thus, a more instructive way of comparing the data is
487 through the power spectral densities of the signals, as shown in Fig. 12 for the transverse velocity
488 component.

489 From Fig. 12, it can be seen that there is good agreement between devices and that the probe
490 is able to resolve the 0.5 Hz waves clearly (Fig. 12(b)). The spectra agree well up to 20 Hz -
491 the Nyquist frequency of the LDV data - and both spectra show a $-5/3$ decay as expected in the
492 inertial subrange of a turbulent flow. There is a small offset between the probe and the LDV
493 signals at low frequencies; this may be due to motion of the probe stem.

494 The power spectral densities of the signals in the transverse and vertical directions are shown
495 in Fig. 13. It can be seen that, again, there is good agreement between the LDV and probe
496 spectra. As with the streamwise spectra, the $-5/3$ roll-off is observed cleanly in all four plots.

497 As expected, the waves do not introduce any significant disturbance in the transverse direction,
498 and neither device gives a spike at 0.5 Hz in Fig. 13(b). In the vertical direction, however, the
499 waves would be expected to generate a substantial disturbance, and this is picked up clearly by
500 both the probe and the LDV in Fig. 13(d) as a sharp spike at 0.5 Hz^2 . The magnitude of this
501 spike is ten times smaller than that of the spike in the streamwise spectrum (Fig. 12(b)), and this
502 explains why it is difficult to discern the 0.5 Hz fluctuations by eye in the vertical velocity trace
503 in Fig. 11(c). The 0.5 Hz component is, however, clearly the major energy-containing frequency
504 in the vertical direction and this is as expected.

505 As well as the spectral content of the turbulent flow, it is useful to know the lengthscales of
506 turbulence present. The standard technique for estimating turbulence lengthscales from single
507 point measurements is to use the autocorrelation function and to define the ‘integral timescale’ as
508 the area under the autocorrelation curve up to the first zero crossing. The integral lengthscale is
509 then defined as the integral timescale multiplied by the bulk flow speed. This method is described
510 in detail by Pope [14].

511 The autocorrelation of the streamwise data from both the LDV and the probe is plotted in
512 Fig. 14 both in clean flow (Figs. 14(a) and (c)) and with waves (Figs. 14(b) and (d)). In each
513 case, the upper plot shows the autocorrelation of data over 90 seconds, while the lower plot
514 shows only the first five seconds, so that the agreement in the zero-crossing can be examined.

²The LDV data shown here was acquired in a separate test to the probe data

515 Looking at Fig. 14(a), it can be seen that the autocorrelation function for both data sets
516 fluctuates over a period of about 25-30 seconds. This is approximately equal to the throughflow
517 time of the tank and therefore could be linked to oscillations in the flow speed controller (which
518 holds the flow nominally constant); long-timescale oscillations in the bulk flow speed are also
519 apparent in the raw velocity traces in Fig 11.

520 Over the shorter period of time shown in Fig. 14(c), the agreement is good, though there is a
521 significant difference in the zero crossing point, and the estimated turbulent lengthscale from the
522 probe data is approximately 25% longer than that obtained from the LDV data. This difference
523 may be due to the spatial offset between the LDV and the probe - although the spectra in Fig 12
524 are similar, the turbulence may be evolving between the two locations, and, if this is the case,
525 the lengthscale would be expected to be longer at the downstream location (the probe) [15].
526 Alternatively, the difference in lengthscale in the streamwise direction could be due to probe
527 motion, as postulated above.

528 Turning now to the autocorrelation data with the waves (Fig. 14(b) and (d)), it can be seen that
529 the signal is dominated by a sinusoid with a period of approximately 2 seconds. This is to be
530 expected: as shown by the spectra, the 0.5 Hz disturbance due to the waves contains substantially
531 more energy than any other fluctuations in the flow and so the autocorrelation is dominated by
532 this frequency. As with the spectra, the agreement between the LDV and the probe is good, with
533 the zero-crossing point in almost exactly the same place in Fig. 14.

534 The autocorrelation of data in the transverse direction is compared in Fig. 15, with the same
535 four plots shown as in Fig. 14. It can be seen the agreement between the LDV and the prototype
536 probe is better in the transverse direction than the streamwise direction. The zero crossing point
537 is also closer to the y-axis, suggesting smaller disturbances are present in the transverse direction
538 than in the streamwise direction. As with the spectra, comparing Figs. 15(c) and (d) it can be
539 seen that the waves make very little difference to the flow in the transverse direction.

540 Finally, the autocorrelation of the probe data in the vertical direction is shown in Fig. 16
541 (LDV data is shown for the wave case in Fig. 16(b) and (d); this data is taken from a separate
542 test). Without waves (Fig. 16(a) and(c)), it can be seen that the zero crossing occurs at a similar
543 time to that observed in the transverse direction, suggesting eddies of a similar size. With waves
544 (Fig. 16(b) and (d)), there is a 0.5 Hz sinusoidal pattern that emerges after the first zero crossing
545 as with the streamwise data, and the agreement between the probe and LDV data is good.
546 Again, this is in line with the spectra, which showed that the waves dominated the spectrum in

547 the vertical direction.

548 From this analysis, it can be seen that the probe agrees with the LDV measurements and gives
549 reliable information on the three-dimensional flow up to frequencies of 20 Hz. A frequency of
550 20 Hz corresponds to a 10 cm gust convecting with the flow - i.e. far smaller than the gusts
551 that are important for tidal turbine design. This result, together with the low cost of the device,
552 means that five-hole probes could be used to obtain high fidelity turbulence measurements at
553 tidal power sites and thus give a vast improvement in the accuracy of unsteady load predictions.

554 XI. FUTURE IMPROVEMENTS

555 The tests with the proof of concept device have shown that a five-hole probe can be used
556 to capture unsteady flow features in a tidal channel flow. There are, however, some further
557 improvements which need to be made in a production-ready device.

558 The main source of error in the measurements from the probe is due to drift in the zero offset
559 of the pressure transducers. The use of higher quality transducers with a smaller pressure range
560 would reduce this error. Alternatively, a cap-type device could be deployed to shield the probe
561 from the flow while a zero reading was taken at regular intervals.

562 Secondly, two further pressure transducers could be added: an additional differential transducer
563 placed out of the flow to measure the hydrostatic pressure gradient and an absolute sensor to
564 give the hydrostatic pressure and therefore the depth of the probe.

565 Thirdly, a compass and tilt-meter would give the orientation of the probe and would enable
566 its precise position and direction recorded while flow data was acquired. There is space in the
567 probe head to house these devices.

568 Fourthly, the calibration procedure must be refined and the generality of each step established.
569 Due to the large scale of the probe relative to a typical aerospace device, geometric variations are
570 likely to have a minimal effect on the calibration map [5]. This hypothesis needs to be verified
571 in tests with several devices over a wider range of flow angles and speeds in order to produce
572 a universal calibration map.

573 Finally, in terms of operability in the marine environment, the data acquisition and power
574 must be integrated so that the probe operates remotely without a cable connecting to the surface.
575 This would be achieved by placing a second PCB and a battery in the probe head, such that the
576 device could be switched on and deployed to acquire data for a set period of time. The probe

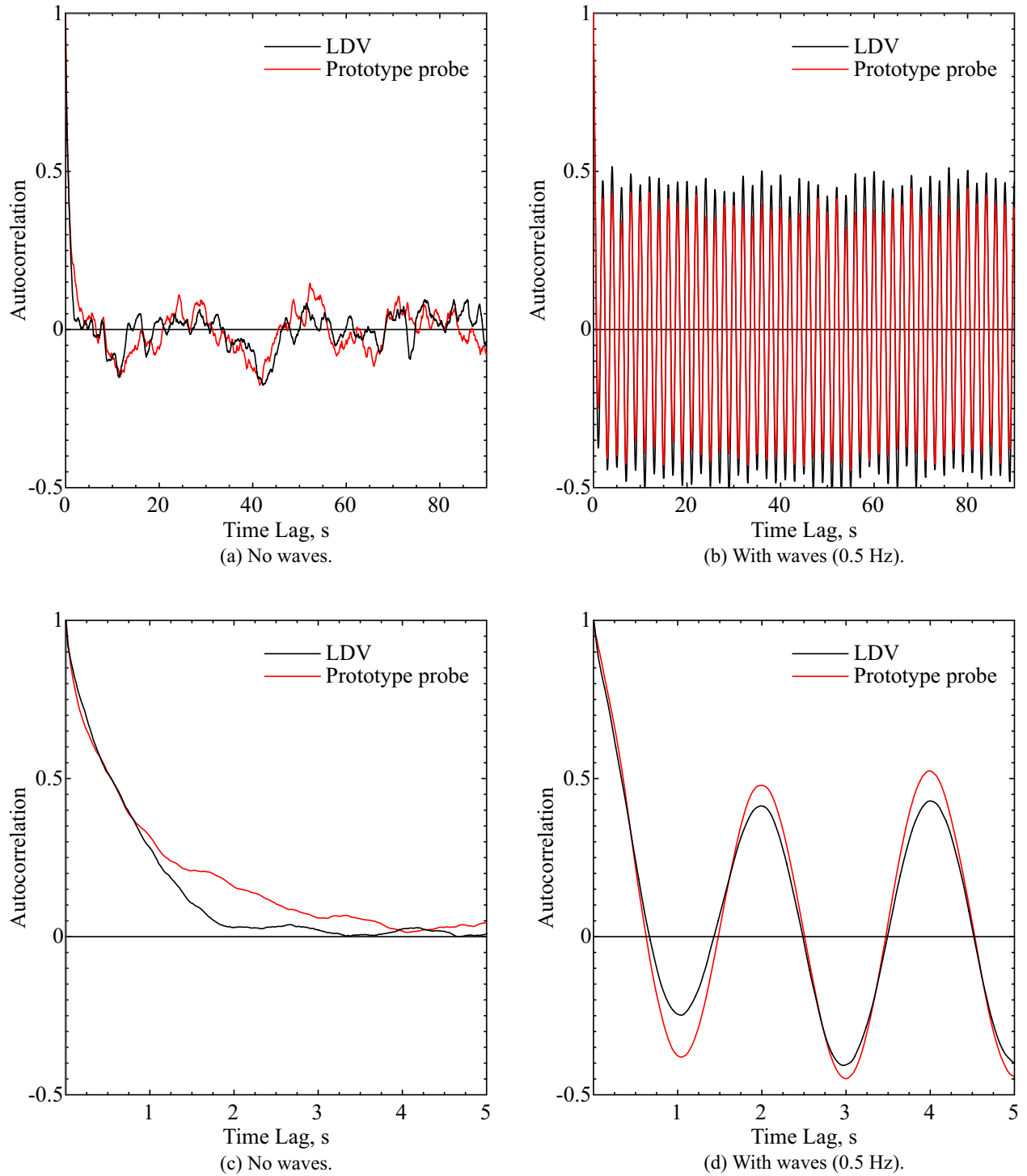


Fig. 14. Comparison of streamwise autocorrelation function from five-hole probe with LDV measurements with and without waves (0.8 m/s).

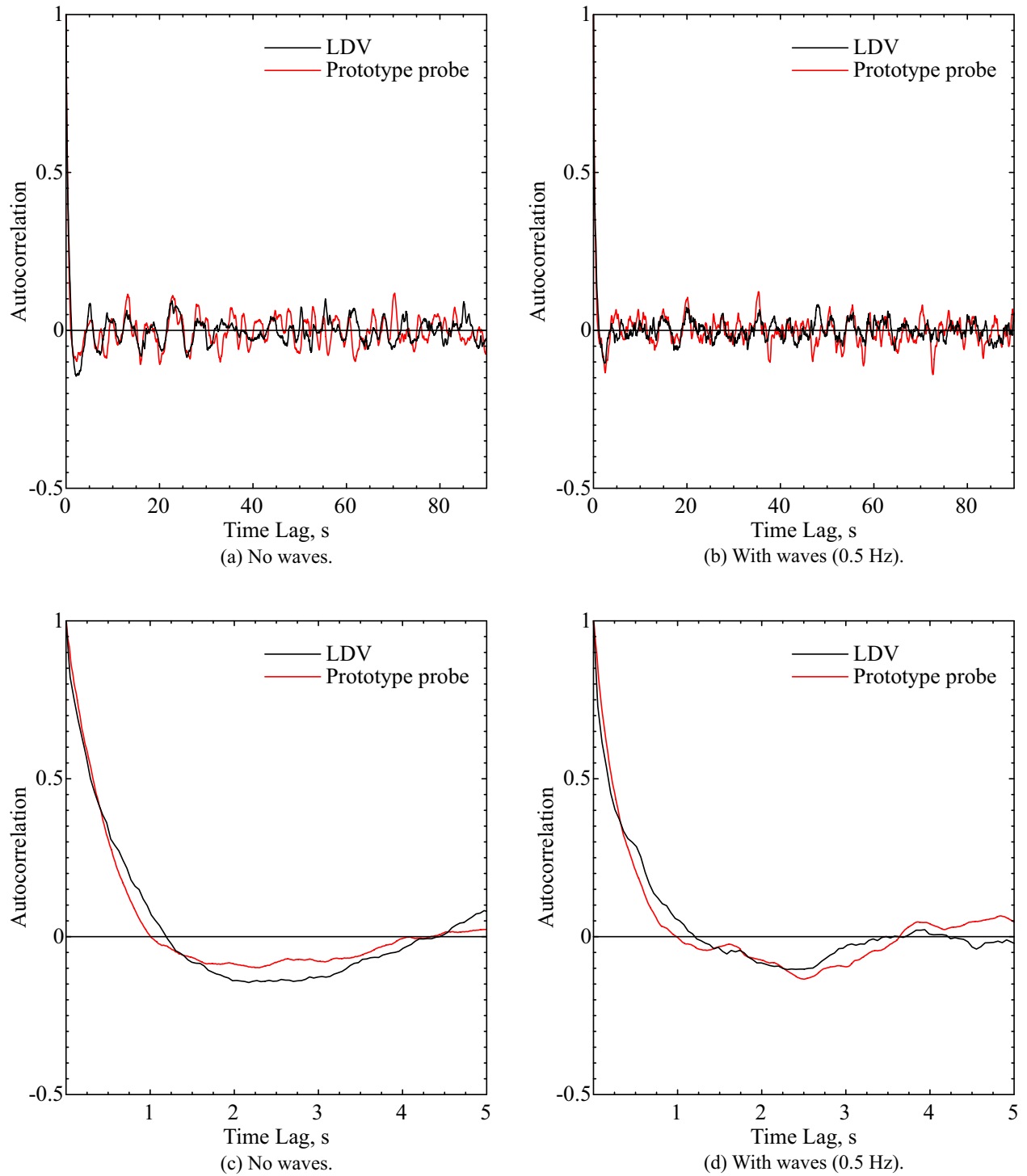


Fig. 15. Comparison of transverse autocorrelation function from five-hole probe with LDV measurements with and without waves (0.8 m/s).

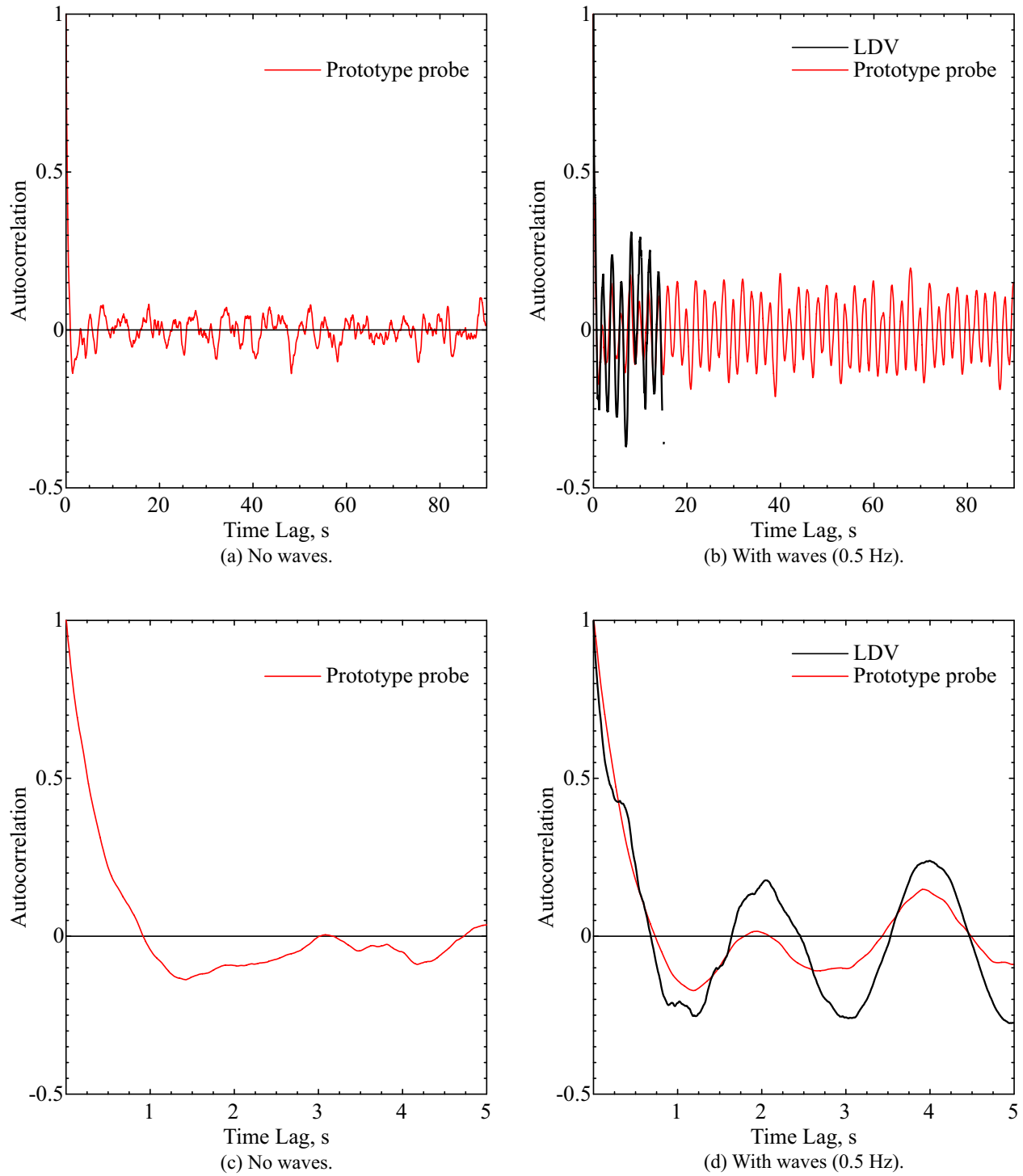


Fig. 16. Vertical autocorrelation function from five-hole probe with and without waves (0.8 m/s).

577 would then be retrieved and data transferred via an IP-68 rated data port. This connection would
578 also allow monitoring and control in a laboratory environment.

579

XII. CONCLUSIONS

580 It has been shown that the unsteady five-hole probe represents a viable, low-cost means of
581 obtaining turbulence measurements in tidal channels. The data provided by such a probe is of
582 huge importance for tidal stream turbine development, where high-fidelity information on the
583 inflow conditions across the whole site is needed in order for accurate fatigue life assessments
584 to be made.

585 The primary difference between traditional five-hole probes used in air and the new marine
586 probe demonstrated here is the novel differential connection which avoids the use of absolute
587 pressure measurements or the need for a local reference pressure. The transducers are installed
588 such that each measures the difference in pressure between one of the four side faces and the
589 central hole. This, along with new calibration coefficients, allows the dynamic pressure to be
590 measured accurately despite its small magnitude relative to the hydrostatic pressure.

591 A prototype probe has been built using off-the-shelf electronic components, with a bespoke
592 amplifier for space reasons. It has been calibrated and tested in a flume tank at 1 m depth with
593 mean flow from 0.4 m/s to 1.6 m/s.

594 The main source of error in the measurements from the probe is due to drift in the zero offset
595 of the pressure transducers, which can cause errors of 5-10% in mean flow speed. If this drift
596 can be accounted for, errors can be reduced to less than 5% of the mean velocity for flow speeds
597 of 0.6 m/s and above. The use of higher quality transducers with a smaller pressure range would
598 further reduce this error.

599 In tests alongside an LDV system, unsteady flow features, including waves, were captured
600 accurately by the probe at frequencies of up to 20 Hz. This is well in excess of the frequencies
601 required for tidal turbine fatigue life design calculations.

602

ACKNOWLEDGMENT

603 The authors would like to thank the staff at Ifremer for their assistance with testing, and Ivor
604 Day and Chris Freeman for their technical help. An earlier version of this work was presented
605 at the XXIII Biennial Symposium on Measuring Techniques in Turbomachinery, Stuttgart, 2016.

REFERENCES

606

- 607 [1] R. U. Guion and A. M. Young, "The frequency response of acoustic doppler current profilers: Spatiotemporal response
608 and implications for tidal turbine site assessment," in *Oceans-St. John's, 2014*, pp. 1–10, IEEE, 2014.
- 609 [2] P. Duquesne, C. Deschênes, M. Iliescu, and G. Ciocan, "Calibration in a potential water jet of a five-hole pressure probe
610 with embedded sensors for unsteady flow measurement," in *Fourth International Conference on Experimental Mechanics*,
611 pp. 752217–752217, International Society for Optics and Photonics, 2009.
- 612 [3] P. Duquesne, G. D. Ciocan, V. Aeschlimann, A. Bombenger, and C. Deschênes, "Pressure probe with five embedded
613 flush-mounted sensors: unsteady pressure and velocity measurements in hydraulic turbine model," *Experiments in fluids*,
614 vol. 54, no. 1, p. 1425, 2013.
- 615 [4] M. J. Dunkley, *The aerodynamics of intermediate pressure turbines*. PhD thesis, University of Cambridge, 1998.
- 616 [5] B. F. Hall and T. Povey, "The oxford probe: an open access five-hole probe for aerodynamic measurements," *Measurement
617 Science and Technology*, vol. 28, p. 035004, jan 2017.
- 618 [6] T. J. Dudzinski and L. N. Krause, "Flow-direction measurement with fixed-position probes," *NASA Technical Memorandum
619 X-1904*, 1969.
- 620 [7] R. Dominy and H. Hodson, "An investigation of factors influencing the calibration of 5-hole probes for 3-d flow
621 measurements," *Journal of Turbomachinery - Transactions of the ASME*, vol. 115, pp. 513–519, 1993.
- 622 [8] R. W. Ainsworth, J. L. Allen, and J. J. M. Batt, "The development of fast response aerodynamic probes for flow
623 measurements in turbomachinery," in *ASME 1994 International Gas Turbine and Aeroengine Congress and Exposition*,
624 pp. V005T15A002–V005T15A002, American Society of Mechanical Engineers, 1994.
- 625 [9] B. Gaurier, P. Davies, A. Deuff, and G. Germain, "Flume tank characterization of marine current turbine blade behaviour
626 under current and wave loading," *Renewable Energy*, vol. 59, pp. 1 – 12, 2013.
- 627 [10] O. D. Medina, F. G. Schmitt, R. Calif, G. Germain, and B. Gaurier, "Turbulence analysis and multiscale correlations
628 between synchronized flow velocity and marine turbine power production," *Renewable Energy*, vol. 112, pp. 314–327,
629 2017.
- 630 [11] G. Zilliac, "Modelling, calibration, and error analysis of seven-hole pressure probes," *Experiments in Fluids*, vol. 14,
631 no. 1-2, pp. 104–120, 1993.
- 632 [12] C. Chondrokostas, R. Willinger, and S. Tsangaris, *Calibration of pneumatic five-hole probes in the free-jet wind tunnel*.
633 PhD thesis, Technical University of Vienna, 2005.
- 634 [13] C. Tropea and A. L. Yarin, *Springer handbook of experimental fluid mechanics*, vol. 1. Springer Science & Business
635 Media, 2007.
- 636 [14] S. B. Pope, *Turbulent Flows*. Cambridge University Press, 2000.
- 637 [15] P. Roach, "The generation of nearly isotropic turbulence by means of grids," *International Journal of Heat and Fluid
638 Flow*, vol. 8, no. 2, pp. 82–92, 1987.